International Journal of Offshore and Polar Engineering (ISSN 1053-5381)

Vol. 30, No. 1, March 2020, pp. 1–10; https://doi.org/10.17736/ijope.2020.jc774

http://www.isope.org/publications/publications.htm

A Blind Comparative Study of Focused Wave Interactions with Floating Structures (CCP-WSI Blind Test Series 3)

Edward Ransley*[1], Shiqiang Yan*[2], Scott Brown[1], Martyn Hann[1], David Graham[1], Christian Windt[3], Pal Schmitt[4], Josh Davidson[5], John Ringwood[3], Pierre-Henri Musiedlak[1], Jinghua Wang[2], Junxian Wang[2], Qingwei Ma*[2], Zhihua Xie*[6], Ningbo Zhang[7], Xing Zheng*[7], Giuseppe Giorgi[8], Hao Chen[9], Zaibin Lin[9], Ling Qian*[9], Zhihua Ma[9], Wei Bai[9], Qiang Chen[10], Jun Zang[10], Haoyu Ding[10], Lin Cheng[11], Jinhai Zheng[11], Hanbin Gu[12], Xiwu Gong[12], Zhenghao Liu[13], Yuan Zhuang[13], Decheng Wan*[13], Harry Bingham[14], Deborah Greaves[1]

[1]University of Plymouth, UK; [2]City, University of London, UK; [3]Maynooth University, Ireland; [4]Queen's University Belfast, UK; [5]Budapest University of Technology and Economics, Hungary; [6]Cardiff University, UK; [7]Harbin Engineering University, China; [8]Politecnico di Torino, Italy; [9]Manchester Metropolitan University, UK; [10]University of Bath, UK; [11]Hohai University, China; [12]Zhejiang Ocean University, China; [13]Shanghai Jiao Tong University, China; [14]Technical University of Denmark

Results from the CCP-WSI Blind Test Series 3 are presented. Participants, with numerical methods, ranging from low-fidelity linear models to high-fidelity Navier–Stokes (NS) solvers, simulate the interaction between focused waves and floating structures without prior access to the physical data. The waves are crest-focused NewWaves with various crest heights. Two structures are considered: a hemispherical-bottomed buoy and a truncated cylinder with a moon-pool; both are taut-moored with one linear spring mooring. To assess the predictive capability of each method, numerical results for heave, surge, pitch, and mooring load are compared against corresponding physical data. In general, the NS solvers appear to predict the behaviour of the structures better than the linearised methods, but there is considerable variation in the results (even between similar methods). Recommendations are made for future comparative studies and development of numerical modelling standards.

INTRODUCTION

Numerical predictions are being used more and more frequently in the design and development of offshore installations. Consequently, there exists an exhaustive range of numerical models, covering the entire spectrum of fluid phenomena (typically with considerable overlap in capability across large groups of existing codes). The usual compromise between computational efficiency and level of the physics being solved, i.e., model "fidelity," still strongly dictates the model used by end users. Despite this, there is no consensus on the required numerical model fidelity for any particular wave–structure interaction (WSI) application, and it is likely that in most cases either important physical phenomena are neglected or excessive computational resources are used. Consequently, if numerical models (particularly high-fidelity ones) are to be used effectively by the industry, a greater understanding of the boundaries of each model's predictive capability is required (Ransley et al., 2016). Furthermore, as demonstrated in the CCP-WSI Blind Test Series 1 (which considered a fixed structure) (Ransley et al., 2019), judging the predictive capability of a model quantitatively is far from trivial; the "quality" of the numerical result tends to be strongly affected by the implementation strategy and experience of the operator, and what constitutes a "good" result depends heavily on the application and the requirements of the end user.

The CCP-WSI Blind Test Workshops have been designed to tackle these issues and raise the necessary questions to maximise the value of future comparative studies. It is hoped this will accelerate the development of numerical modelling standards in WSI applications and increase the uptake of state-of-the-art numerical techniques by industry. These workshops bring together numerical modellers from the WSI community and assess the numerical codes currently in use by inviting participants to simulate a set of bespoke physical validation experiments, covering a range of relevant complexities, without prior access to the physical measurements. The "blind" nature of the CCP-WSI Blind Test Workshops allows for assessment of numerical methods, without artificial manipulation of the results to match the physical measurements (which clearly represents a potential source of bias in traditional comparative studies). Furthermore, to enable contributions using all WSI modelling strategies, no constraints are applied to the computational implementation, and participants are encouraged to use "best practice" to generate their solutions. However, as was made clear in the CCP-WSI Blind Test Series 1 (Ransley et al., 2019), participants can have a very different idea of what "best" practice is, and this can result in distinct differences in the quality of the solution, even when comparing similar models. This does complicate the assessment, but it is important in demonstrating to industry end users the risk posed by a lack of best practice guidelines (without which the appropriate constraints are unknown anyway). It is, therefore, critical that this effort continues and complements other efforts (Wendt et al., 2019) to help standardise numerical modelling practices. Only then will we make progress

*ISOPE Member.

Received November 19, 2019; updated and further revised manuscript received by the editors January 27, 2020. The original version (prior to the final updated and revised manuscript) was presented at the Twenty-ninth International Ocean and Polar Engineering Conference (ISOPE-2019), Honolulu, Hawaii, June 16–21, 2019.

KEY WORDS: Code comparison, numerical validation, CFD, PIC, linear potential theory, nonlinear Froude-Krylov, hybrid codes, cylinder, moonpool, wave energy converter, heave, surge, pitch, mooring load.

towards understanding the true predictive capability of different models, converge towards a manageable suite of tools, and extend the real benefits of this effort to industry.

The CCP-WSI Blind Test Series 3 was held in conjunction with the ISOPE conference, in collaboration with the IHC, and builds on the Blind Test Series 1 (Ransley et al., 2019), in which participating numerical models were compared in terms of pressure and runup on a fixed FPSO model in focused waves. The release of the Series 3 test cases was made in September 2018, and the showcase event was held over a series of special sessions at the 29th annual ISOPE conference in Honolulu, Hawaii (June 2019). More information on the CCP-WSI Blind Tests is available on the CCP-WSI website at http://www.ccp-wsi.ac.uk/blind_test_workshops where supporting material is available, including complementary references, photographs from the experiments, and other related resources.

TEST CASES

The CCP-WSI Blind Test Series 3 test cases consist of three focused wave events, with a range of steepness, $kA = 0.13$–0.21, incident upon two separate, floating structures: a hemispherical-bottomed buoy (Geometry 1) and a truncated cylinder with a cylindrical moon-pool (Geometry 2). Here, k is the wave number associated with the peak period, T_p, of the underlying energy spectrum of the wave, and A is the crest amplitude of the crest focused wave, assuming linear superposition of the underlying wave components. All waves are nonbreaking in isolation. The purpose of these particular test cases is to measure the predictive capability of a wide range of numerical WSI codes as a function of wave steepness and geometric complexity (Geometry 2 is considered to be more complex due to the "internal" body of water within the moon-pool), and to evaluate the required model fidelity when assessing critical design factors, such as the motion of floating structures and loads in a mooring system.

Both structures are axis-symmetric with their mooring attachment located level with the bottom of the structure on the axial line; in the case of Geometry 2, a frame of three 20-mm-wide, 3-mm-thick steel bars is welded to the structure to enable the mooring attachment. The two buoys are designed to resemble simple, scale-model, wave energy converters (WECs) and are ballasted to have similar drafts and water-plane areas (in an attempt to isolate the effect of the moon-pool and relate this to the predictive capability of the numerical models). The dimensions and mass properties of the two structures are given in Fig. 1 and Table 1, respectively, where z_{CoM} is the axial (vertical) distance to the CoM, from the bottom of the buoy/mooring attachment,

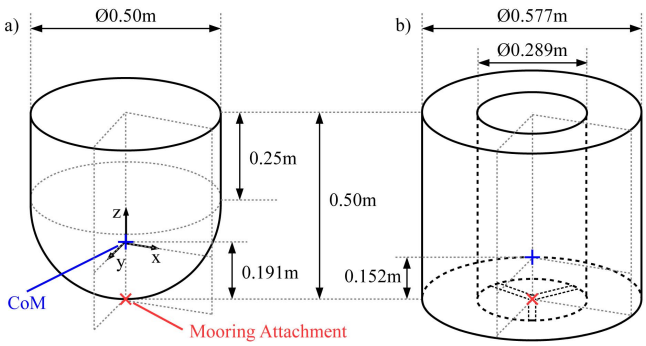

Fig. 1 Dimensions, including the positions of the centre of mass (CoM) and mooring attachment, for (a) Geometry 1, and (b) Geometry 2

	Mass (kg)	z_{CoM} (m)	I_{xx} (kgm^2)	I_{yy} (kgm^2)	I_{zz} (kgm^2)
G1	43.674	0.191	1.620	1.620	1.143
G2	61.459	0.152	3.560	3.560	3.298

Table 1 Mass properties of Geometry 1 (G1) and Geometry 2 (G2)

	Draft (m)	Mooring pretension (N)	z-position of CoM (m)
G1	0.322	32.07	−0.131
G2	0.330	31.55	−0.178

Table 2 Key values with structures at rest

and I_{zz} is the moment of inertia about the vertical (z) axis. The moments of inertia corresponding to the other two geometric axes, I_{xx} and I_{yy}, are given relative to the CoM of each of the structures. Complementary work involving Geometry 1 can be found in Hann et al. (2015) and Ransley et al. (2017).

In all cases, the structure is taut-moored using the same linear spring mooring with a stiffness of 67 N/m and a rest length of 2.199 m. Table 2 gives some key parameters when the structure is at rest ($z = 0$ corresponds to the still water level).

In each experiment, the six-degrees-of-freedom (6DOF) motion of the structure is recorded using an optical motion capture system, the inline load in the mooring is recorded using a single-axis load cell attached to the basin floor via a universal joint, and the surface elevation in the vicinity of the structures is recorded using an array of resistive wave gauges.

Experimental Setup

Basin Geometry. The experiments were performed in the COAST Laboratory Ocean Basin (35 m long × 15.5 m wide) at the University of Plymouth, UK. The basin has 24 flap-type, force-feedback-controlled wavemakers (hinge depth of 2 m). The water depth at the wavemakers is 4 m, and there is a linear slope

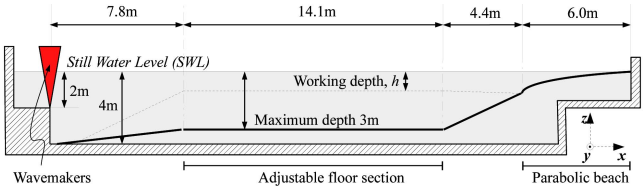

Fig. 2 Schematic of the COAST Laboratory Ocean Basin

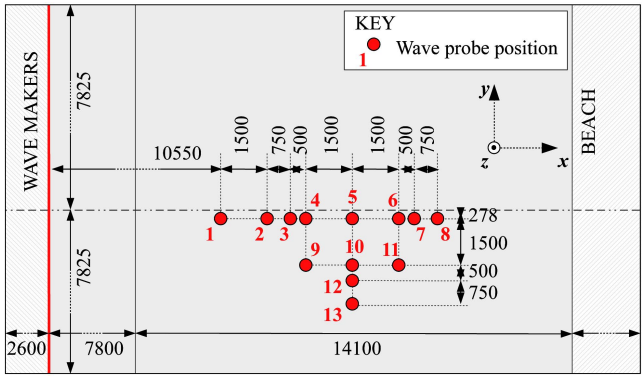

Fig. 3 Wave gauge layout; wave probe position 5 corresponds to the position of the structure's CoM in cases with the structure included (all dimensions in mm; not to scale).

Case	$A_n\,(m)$	f_p (Hz)	h (m)	H_s (m)	kA
1BT3	0.2	0.4	3.0	0.274	0.129
2BT3	0.3	0.4	3.0	0.274	0.193
3BT3	0.32	0.4	3.0	0.274	0.206

Table 3 Wave conditions used in the CCP-WSI Blind Test Series 3

to the working area where the water depth, h, was set to 3.0 m. At the far end of the basin, there is a parabolic absorbing beach (Fig. 2).

Structure Position and Wave Gauge Layout. Thirteen wave gauge positions were used, according to Fig. 3. Position 5 corresponds to the rest position of the buoy(s) (with the structure in place, gauge 5 was removed, but the same number system was maintained).

Test Program and Wave Parameters

For each test case, the incident waves were generated using paddle control software that is designed to reproduce the desired free-surface elevation by applying various corrections to account for the change in water depth in front of the wave paddles and the nonlinear propagation of the wave fronts. Each wave was created using linear superposition of 244 wave fronts with frequencies evenly spaced between 0.101563 Hz and 2 Hz. All waves in the CCP-WSI Blind Test Series 3 are unidirectional, nonbreaking, and crest-focused; i.e., each of the contributing wave components has a phase of 0 at a theoretical focus location, x_0. The amplitudes of the components are derived by applying the NewWave theory (Tromans et al., 1991) to a Pierson–Moskowitz spectrum, with the three waves in Series 3 differing only by crest height; i.e., the waves progressively increase in steepness, from 1BT3 to 3BT3, but retain the same underlying frequency content (Table 3). Each wave front is then transformed back to the position of the wave paddles by the control software, and x_0 is iteratively adjusted (as described by Hann et al., 2015) to pragmatically ensure "focusing," that is, a symmetric event, at the position coincident with the centre of the structure(s), i.e., wave gauge 5.

Released Data

The CCP-WSI Blind Test Series 3 is a blind validation of numerical WSI codes. Consequently the only physical measurement data released to participants, prior to submission, were the surface elevation records from a series of empty tank tests, i.e. without the structure in place, at the wave gauge positions in Figure 3. This data is deemed sufficient to reproduce the incident waves in cases including the structure, as the same wave-maker signals are used. The remaining physical measurements were not released until after all participants had submitted their final results, and it is these 'blind' results that are reported in this paper.

Physical Measurement Errors and Experimental Limitations.

As discussed in the CCP-WSI Blind Test Series 1 (Ransley et al., 2019), it is crucial that the errors/uncertainties in the physical validation experiments are well understood if a conclusive, quantitative assessment of predictive capability is to be made. As is the case here, it is recommended that bespoke experiments are conducted with the sole purpose of numerical model validation. Furthermore, it must be recognised that, in order to differentiate the capabilities of high-fidelity models, an equally "high-fidelity" physical data set is required. It is too often the case that comparative studies, and numerical validation activities, fail to provide conclusive measures of predictive capability due to a less-than-thorough understanding of the physical model setup and experimental errors, leading to prohibitive uncertainties in the validation data. As in Series 1, the nonbreaking, compact focused wave groups help to minimise sources of random error associated with the wave generation, and the repeatability of the waves is good (2.5% maximum relative standard deviation, σ_{rel}, in the crest height of the steepest wave, over 5 repeats, and much less for the less steep waves, ≈1%). The repeatability of the body motion is also good with a σ_{rel} in the maximum heave, surge, and pitch of 0.3%, 1.2%, and 1.8%, respectively. Systematic errors, particularly those present in the description of the structure and mooring system, are the biggest concern in these tests: the precise dimensions of the structures and mooring line may differ by less than 1%, but there is greater uncertainty in the mass properties of the two structures, and a series of assumptions have been made about the mooring line. The masses and moments of inertia of the two structures have been measured using a compound pendulum "swing" test (Hinrichsen, 2014) and verified against outputs from a comprehensive computer-aided design (CAD) model. However, due to practical limitations over the optimal pendulum lengths, the precision of the swing test is uncertain and the accuracy questionable, particularly when measuring the moments of inertia. Consequently, the potentially erroneous description of the moments of inertia may lead to discrepancies between the physical and numerical results, particularly in the rotational behaviour, i.e., pitch. However, since all the participants use the same mass properties, convergence is, at least, expected between the numerical models. Lastly, neither the mass nor drag properties of the mooring line are known; participants are advised to assume the mooring is massless and offers no resistance to the fluid. Furthermore, the universal joint on the basin floor is assumed to be idealised. Consequently, any dynamic behaviour/inertia effects or drag on the mooring that were present in the physical experiments will not be captured in the numerical models.

NUMERICAL METHODS

Participating Codes

The CCP-WSI Blind Test Series 3 involved 32 participants from 14 academic institutions. There were 10 submissions ranging from linear potential theory (LPT) to NS solvers, including hybrid (coupled) methods, particle methods, finite difference methods (FDM), finite element methods (FEM), and finite volume methods (FVM). No constraints on the implementations of the models were applied as part of the test. Each method is described below and summarised in Table 4.

PIC Method (in-house). This model employs the hybrid Eulerian–Lagrangian PIC method to solve the incompressible NS equations for single-phase free-surface flows. Fluid–solid interaction is incorporated via a Cartesian cut-cell-based, two-way coupling algorithm (Q Chen, Zang, et al., 2019). Waves are generated using a piston-type wave paddle with the displacement, based on first-order wavemaker theory, derived iteratively by adjusting the theoretical focus location and amplitude. Wave absorption is via an improved relaxation approach (Q Chen, Kelly, and Zang, 2019). The computational domain is 21 m long, 6 m wide, and 4 m tall and consists of ∼32 million cells (edge length = 0.025 m) and ∼189 million particles. Dynamic time-stepping is used ($Co = 0.5$). Laminar flow is assumed; i.e., no turbulence modelling is employed. Computation is performed on 160 × 2.6 GHz cores.

Code ref.	Discret. scheme	Theory	Free-surface treatment	Turbulence treatment
PIC (in-house)	FDM + meshless	NS	MAC + (1-phase)	laminar
OpenFOAM (source-term)	FVM	NS	VOF	laminar
Hybrid FNPT/NS (in-house)	FEM/ FVM	FNPT/ NS	1-phase/ VOF	inviscid/ laminar
LPT+WAMIT (in-house)	BEM	LPT/ NS	linearised	inviscid
Hybrid FNPT/SPH (in-house)	FEM SPH	FNPT	single-phase	inviscid
NS Solver (FDM) (in-house)	FDM	NS	VOF	LES (SMA)
OpenFOAM (overset)	FVM	NS	VOF	RANS (SST)
Nonlinear Froude-Krylov	Analytical	LPT	—	—
OpenFOAM (waves2Foam)	FVM	NS	VOF	laminar
NS Solver (FVM) (in-house)	FVM	NS	VOF	laminar

Table 4 Summary of numerical methods used by participants

OpenFOAM Using Source-term. This method uses the open-source, FVM-based OpenFOAM (v4.1) and solves the two-phase, incompressible, Reynolds-averaged NS (RANS) equations using volume of fluid (VOF) interface capturing (Rusche, 2002). Body motion is accommodated via dynamic mesh deformation. Incident waves are generated using an impulse source method (Schmitt et al., 2019) with the required source term determined via an iterative calibration method. Wave absorption is achieved via a numerical beach implementation (Schmitt and Elsaesser, 2015). The computational domain is 28.75 m long, 7.825 m wide (utilising a symmetry-plane), and 6 m tall (3 m of air phase) and consists of ∼1 million cells (edge lengths = 1.9 m–0.015 m). A fixed time-step of 0.002 s is used. Laminar flow is assumed. Computation is performed on 23×2.4 GHz cores (Windt et al., 2019).

Hybrid FNPT FNPT/NS Method (in-house). The hybrid FNPT/NS solver, qaleFOAM, combines the FNPT model, QALE-FEM (Ma and Yan, 2006, 2009), with OpenFOAM's VOF, NS solver, using domain decomposition and a coupling boundary (Li et al., 2018). Body motion (in NS domain) is via mesh deformation. Wave generation and absorption are achieved (in FNPT domain) using self-adaptive wavemakers. The FNPT domain mimics the physical wave basin (Fig. 2) with a characteristic cell size of 0.075 m. The NS domain is 6 m long, 3 m wide, and 4.5 m tall and consists of 613,000 cells (edge lengths = 0.02 m–0.1 m). Dynamic time-stepping is used ($Co = 0.4$). Laminar flow is assumed. 16×2.4 GHz cores are used (Yan et al., 2020).

LPT + WAMIT Method (in-house). In this method, linear potential theory (LPT) is used to compute the frequency-domain response of the body, including the mooring line as a linear spring (WAMIT, 2019; Bingham, 2019). The incident waves are assumed to be a linear superposition of the Fourier coefficients from the measured surface elevation signal at probe 5 in the empty tank test. The geometry is represented exactly using high-order B-splines with 54 unknowns in total. Computation is performed using 4×2.5 GHz cores. Only cases involving Geometry 1 were simulated using the LPT method.

Hybrid FNPT/SPH Method (in-house). This method couples a fully Lagrangian, mesh-free, smooth particle hydrodynamics (SPH) solver (Zheng et al., 2014) with the FNPT solver, QALE-FEM (Ma and Yan, 2006). The moving body boundary is simulated by using layers of dummy particles. Wave generation, and the mesh in the FNPT domain, are as in the Hybrid FNPT/NS method. The SPH domain is 10 m long and 1.2 m wide with ∼1 million particles. Dynamic time-stepping is used ($Co = 0.2$). Laminar flow is assumed. Computation is performed on 16×3.2 GHz cores. Only case 2BT3 (both geometries) was simulated using this method (Zhang et al., 2019).

NS Solver Using FDM (in-house). NEWTANK uses the FDM to solve the spatially averaged Navier–Stokes (SANS) equations for two incompressible fluids using a VOF scheme. The interaction between the fluid and structure is simulated via a virtual boundary force (VBF) method (Liu and Lin, 2009; Lin et al., 2016). Waves are generated using an expression-based boundary condition based on linear superposition of components derived from the theoretical wave descriptions. Wave absorption is via an artificial damping scheme (Park et al., 1999). The computational domain is 10 m long, 3 m wide, and 4 m tall and consists of ∼0.56 million cells (edge length = 0.02 m–0.66 m). Dynamic time-stepping is used ($Co = 0.3$). Laminar flow is assumed. Computation is performed on 16×2.3 GHz cores (Cheng et al., 2019).

OpenFOAM Using Overset Meshing. This method is based on OpenFOAM (v1706) and solves the RANS equations for two incompressible fluids using a VOF scheme. Overset meshing functionality is applied to accommodate the moving boundary patch (H Chen et al., 2019a). The waves are generated and absorbed using IHFOAM (Higuera et al., 2013). The incident waves are generated based on the second-order irregular wave theory where the components are derived from the given theoretical spectrum. The computational domain is 25 m long, 6 m wide, and 4 m tall (1 m of air phase) and consists of 4.5 million cells (edge length = 0.011875 m–0.25 m). Dynamic time-stepping is used ($Co = 0.35$). The k-ω SST turbulence model is applied. Computation is performed using 64×1.7 GHz cores (H Chen et al., 2019b).

Nonlinear Froude-Krylov. This numerical method implements nonlinear kinematics and nonlinear Froude–Krylov force calculations in a linear potential theory-based framework (Giorgi and Ringwood, 2018a). The waves are a linear superposition of components derived from the surface elevation at probe 5 in the empty tank tests, propagated using linear dispersion and including Wheeler-stretching (Giorgi and Ringwood, 2018b). A fixed time-step of 0.04 s is used. No viscous drag correction is included (as this was not provided). The algorithm is run on one 3.5 GHz core (Giorgi, 2019).

OpenFOAM Using waves2Foam. This method is based on OpenFOAM (v5.0) and solves the RANS equations for two incompressible fluids using a VOF scheme (Rusche, 2002). Body motion is accommodated via dynamic mesh deformation. Incident waves are generated using an expression-based boundary condition, formed from the linear superposition of wave components derived using an FFT of the surface elevation at probe 1 in the empty tank test. Wave absorption is achieved using the relaxation zone approach (Jacobsen et al., 2012). The computational

domain is 25 m long, 15.5 m wide, and 6 m tall and consists of ∼11 million cells (edge lengths = 0.5 m–0.025 m). Dynamic time-stepping is used ($Co = 0.5$). Laminar flow is assumed. Computation is performed on 128 × 2.5 GHz cores (Brown et al., 2019).

NS Solver Using FVM (in-house). naoe-FOAM-SJTU (in-house code based on OpenFOAM) solves the two-phase, incompressible RANS equations using FVM and a VOF interface capturing scheme (Wang et al., 2019). Body motion is accommodated via dynamic mesh deformation. Incident waves are generated using an expression-based, Dirichlet-type boundary condition derived from the theoretical wave descriptions. Wave absorption is via an additional source term in the governing equations (a sponge layer approach). The computational domain is 27 m long, 8 m wide, and 6 m tall (2 m of air) and consists of ∼2.3 million cells (edge lengths = 0.1 m-0.005 m). A fixed time-step of 0.008 s is used. Laminar flow is assumed. Computation is performed on 20 × 2.8 GHz cores (Liu et al., 2019).

RESULTS AND DISCUSSION

Time Series Analysis

Incident Waves. In addition to time series of the heave, surge, pitch, and mooring load, it was requested that participants also submit time series data for the surface elevation, at positions 1, 3, 5, and 8 (Fig. 3), in an empty tank simulation of each wave case. The submissions for the intermediate steepness wave, 2BT3, at the focus position (probe 5) are shown, along with the experimental measurement, in Fig. 4.

As the physical data were available for the empty tank tests and the simulations are significantly simplified, it was anticipated that submissions (particularly those utilising similar methods) would be approximately equal in terms of their reproduction of the experimental result at probe 5, i.e., the "target" location (Fig. 4). However, although there is a group that demonstrates very good reproduction, in general there is noticeably high variation in the quality of the reproduction across the submissions. Ignoring the linearised methods, which effectively have perfect reproduction at probe 5, the variation in the NS solvers clearly demonstrates a difference due to the wave generation/implementation strategy, and in some cases, there are significant discrepancies with respect to the experimental data. When viewed in frequency-space, the differences typically manifest themselves as an overestimation of the energy density at the peak frequency, except in the case of the OpenFOAM (source-term) method, which appears to underestimate the peak, predicts a higher peak frequency, and has some curious additional frequency content. At the other probe locations, there is even more spread in the results (probably due to the iterative "tuning" methods used by some participants concentrating only on the target, probe 5), and the LPT shows considerable discrepancies upstream, demonstrating that the propagation of the waves considered here cannot be described properly by linear theory. These observations (already) demonstrate a need for standardisation in numerical wave generation practices; it is reasonable to assume that the quality of the reproduction in the empty tank cases is strongly correlated with the reproduction in the cases with the structure present (at least for those methods that are required to simulate the propagation of the incident waves). This also makes judging the predictive capability of the models, in the cases with a structure, far more challenging compared to a scenario in which all models generate the incident waves with the same degree of accuracy. There is no obvious trend in the quality of the reproduction as a function of wave steepness.

Heave displacement. Figure 5 shows the heave displacement of Geometry 1's CoM when subject to the intermediate steepness wave, 2BT3. As anticipated (other than some curious exceptions attributed to additional implementation issues), the quality of the heave displacement prediction from the NS solvers resembles closely that of the surface elevation reproduction in Fig. 4; i.e., those methods that have reproduced the waves well also reproduce the heave motion well. The linearised models (including the nonlinear Froude-Krylov method) display some discrepancies in heave displacement and, when viewed in frequency-space, noticeable additional frequency content. However, in general, the prediction of heave displacement is reasonably good across all model fidelities. This is possibly because, in these cases, heave motion may be dominated by inertia and restoring forces (i.e., hydrostatic force, weight, and mooring stiffness) and hence may not be sensitive to some errors in the hydrodynamic forces. In the case of heave displacement, there is no obvious difference in the accuracy with respect to geometry. Again, there is no obvious trend in the quality of the reproduction as a function of wave steepness.

Surge Displacement. Figure 6 shows the surge displacement of Geometry 1's CoM when subject to the intermediate steepness wave, 2BT3. There is noticeably more spread in the quality of the reproduction, particularly after the main wave crest has passed, i.e., during the mean/slow "drift" motion attributed to mean drag and second-order subharmonics (Yan and Ma, 2007; Ma and Yan, 2009). For NS methods, which included these nonlinearatities, those that have reproduced the incident wave well have generally reproduced the surge motion well. As expected, the LPT model does not predict any drift motion as no nonlinear effects

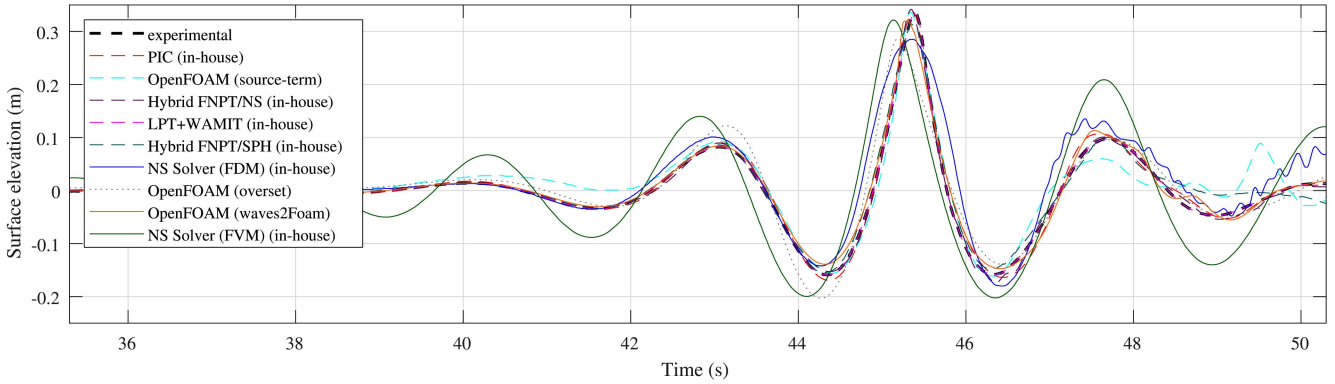

Fig. 4 Surface elevation at the target position, probe 5, from the empty-tank test of the mid-steepness wave, 2BT3. Physical measurements are plotted using a black dotted line; numerical submissions, from all participants, are shown using coloured lines.

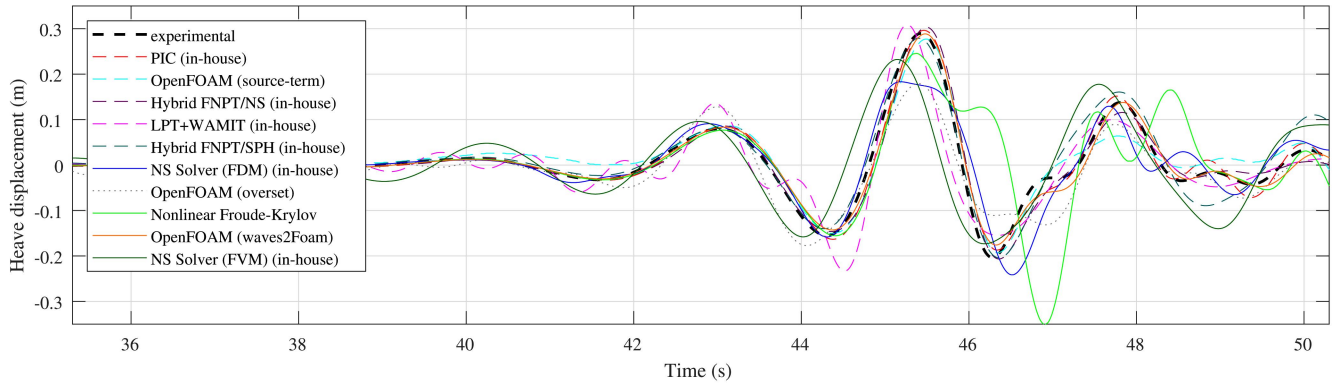

Fig. 5 Heave displacement of Geometry 1's CoM when subject to the mid-steepness wave, 2BT3. Physical measurements are plotted using a black dotted line; numerical submissions, from all participants, are shown using coloured lines.

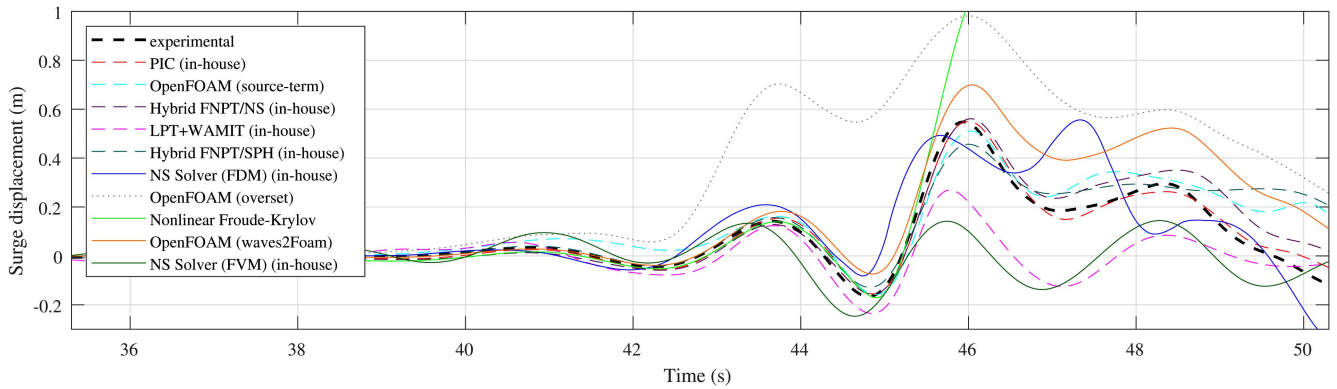

Fig. 6 Surge displacement of Geometry 1's CoM when subject to the mid-steepness wave, 2BT3. Physical measurements are plotted using a black dotted line; numerical submissions, from all participants, are shown using coloured lines.

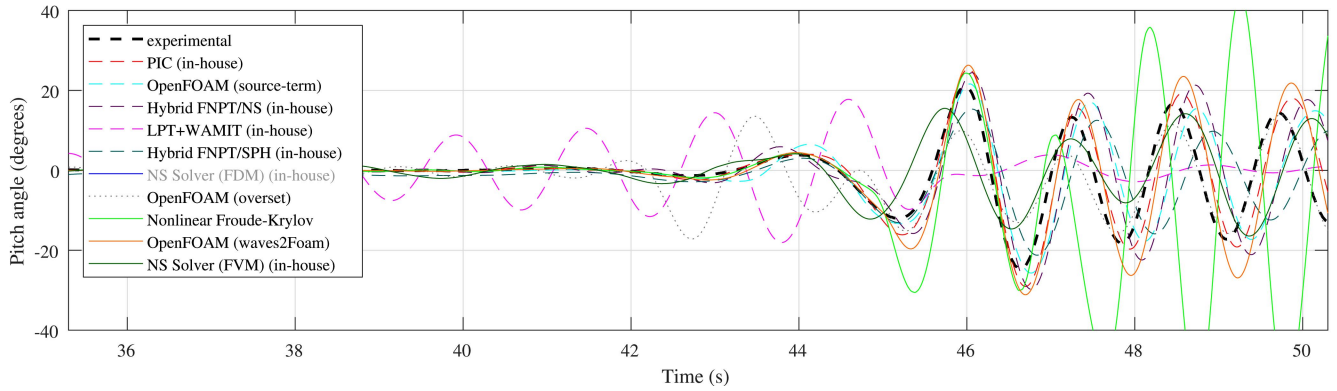

Fig. 7 Pitch angle (according to the left-hand rule) of Geometry 1 when subject to wave 2BT3. Physical measurements are plotted using a black dotted line; numerical submissions, from all participants, are shown using coloured lines.

are included; the nonlinear Froude-Krylov includes the necessary coefficients to predict the drift motion but, in these cases, tends to overestimate this considerably (possibly due to exclusion of viscous drag corrections or assumed linear wave dispersion). One observation with respect to the NS solvers is that the method using overset meshing for the body motion (OpenFOAM (overset)) displays considerable discrepancies in the surge motion. As with heave, there is no obvious trend in the quality of the predictions when comparing the two geometries; however, it is possible that, when viewed in frequency-space, there is an improved capture of high-frequency surge components in the Geometry 2 case, which is unexpected. Again, there is no obvious trend in the quality of reproductions with respect to wave steepness.

Pitch Angle. Figure 7 shows the pitch angle of Geometry 1 when subject to the intermediate steepness wave, 2BT3. In general, during the wave loading event, i.e., up to 46 s here, the NS solvers that reproduced the incident wave well also reproduce the pitch well. However, after 46 s, large variations between these NS solvers are observed in the predicted "free-decay" of the structures, with a tendency for the natural frequency to be apparently underestimated. As noted earlier, possible inaccuracies in the specified mass properties of the structures may explain differences between the numerical predictions and the physical measurements, particularly for pitch motion. However, there is no clear convergence of the pitch natural frequency despite all numerical models specifying the same mass properties. The LPT method clearly struggles with pitch here, with the structure being

excited in pitch much earlier than expected. It is suspected that this is due to the inherent nonlinearity in the incident wave and the failing of linear superposition to predict the free-surface elevation spatially. The nonlinear Froude-Krylov method works well during the wave loading but greatly overestimates the amplitude of the pitch motion after the wave passes; i.e., it greatly underestimates the pitch damping. The pitch results offered by the NS Solver (FDM) have been omitted to an apparent post-processing issue. Again, the OpenFOAM (overset) method displays some odd behaviour, and pitch motion is excited noticeably earlier than it should be (for both geometries). However, at this point, it is worth noting that the three degrees of freedom considered (heave, surge, and pitch) are likely to be strongly coupled with one another in reality, so observed discrepancies in one are likely to cause (and be a cause of) discrepancies in the other two and thus should not be considered in isolation. Again, there is no obvious trend in the predictave capability of the models as a function of wave steepness. Compared to Geometry 1, Geometry 2 displays much greater pitch damping. This is perhaps to be expected due to the flat base of Geometry 2 and associated sharp edges, but also the potential for "sloshing" in the moon-pool, which has been linked consistently with similar motion-damping. Qualitatively, the accuracy of the predicted pitch motion appears to be reduced for Geometry 2, which may be evidence that the additional geometric complexity and associated "internal" fluid volume do represent a scenario that can be used to differentiate the required numerical fidelity.

Mooring Load. Unsurprisingly, in these cases, the mooring load is dominated by the vertical motion, i.e., heave. Consequently, the quality of the numerical reproductions generally mimics that of the heave response and, therefore, the surface elevation reproduction (with the exception of the nonlinear Froude-Kyrlov code, which has significant issues related to its overestimation of the surge motion). Therefore, again, there is no obvious trend in the predictive capability of the codes as a function of either the wave steepness or the geometric complexity. However, one concern raised is that there appear to be considerable issues with predicting the rest tension in the mooring, despite this being specified in the test description.

Quantitative Analysis

In an attempt to uncover any underlying trends and provide a quantitative estimate of predictive capability, the normalised root mean squared (RMS) error in the submitted data has been calculated. As discussed in Ransley et al. (2019), an RMS is a relatively basic analysis tool that reduces the time series data to a single-number representation of the quality of the prediction. Although convenient, this obscures large amounts of (potentially valuable) information about the reproduction and can lead to bias in favour of those solutions that have good phase agreement. Furthermore, the RMS is an "absolute" value that is influenced strongly by the underlying signal and can also be highly sensitive to the window of time over which it is calculated. This makes comparing RMS values across different cases difficult without "normalisation." The RMS values calculated here have been normalised by the standard deviation of corresponding physical data set. It is believed that this normalisation strategy is more appropriate than one based on a discrete maximum, as the normalisation factor considers the behaviour over the entire analysis window and, provided the RMS and standard deviation are over the same analysis window (in this case, 35.3 s–50.3 s), this normalised RMS value should demonstrate some independence from the length of window used.

Figure 8 shows the normalised RMS (NRMS) in the heave displacement, surge displacement, and pitch angle versus the NRMS

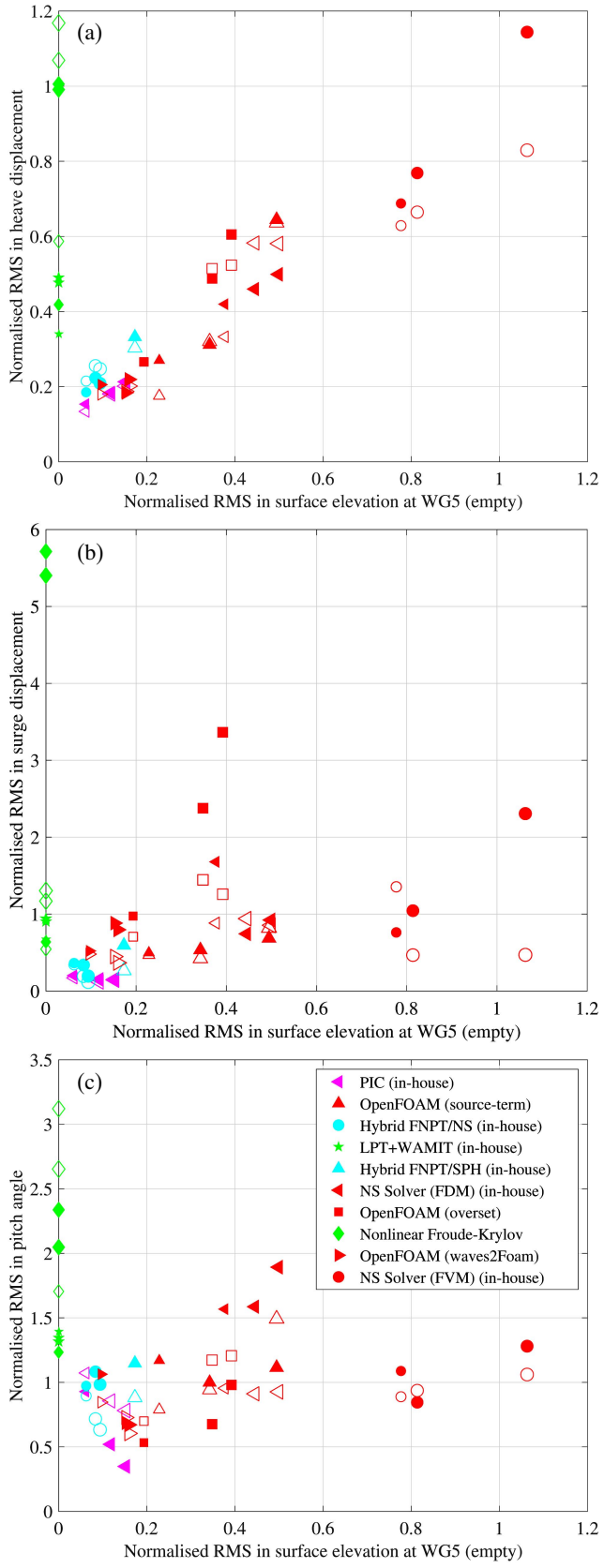

Fig. 8 Normalise RMS error (w.r.t. the experimental data) in the (a) heave displacement, (b) surge displacement, and (c) pitch angle vs. NRMS error in the surface elevation at wave probe 5 (during empty tank tests). Filled markers represent Geometry 1; open markers represent Geometry 2. Marker sized scaled by wave steepness, kA.

in the surface elevation predicted at wave probe 5 in the empty tank tests. The data have been colour-coded according to the underlying theory/method; i.e., red symbolises NS solvers, green symbolises methods based on linear potential theory, cyan symbolises hybrid methods, and magenta symbolises the PIC method; filled markers represent cases involving Geometry 1, and open markers represent those involving Geometry 2; the marker sizes have been scaled according to the wave steepness, kA.

As anticipated from the time series data above, Fig. 8a shows a clear correlation between the NRMS in the heave displacement and the NRMS in the surface elevation at probe 5 (for the methods modelling the wave propagation). In fact, for most of the methods, the trend is nearly linear with a one-to-one relationship; i.e., an increase in the NRMS of the predicted free-surface elevation corresponds to the same increase in the NRMS of the heave displacement. Curiously, there is a group of methods with a slightly inferior trend; i.e., the NRMS in heave increases more rapidly with the NRMS in the surface elevation, and this group contains all of the hybrid method results. Figure 8a also shows that there appears to be a clear intercept of the data at the y-axis, suggesting that even with perfect reproduction of the surface elevation, a finite NRMS (of ∼0.1) in heave displacement will still be observed. Perhaps this suggests that if all the methods (excluding those based on linear theory) reproduced the waves equally well, they would all return an NRMS in the heave displacement of ∼0.1; i.e., they all have the same predictive capability for heave displacement (in the cases considered here), and the ∼0.1 NRMS could represent either the present limitation of modern numerical modelling capabilities or a systematic error in the description of the physical experiment. It can also be seen that, for many of the methods, the NRMS in heave increases with the wave steepness, suggesting that the predictive capability of the codes is a function of wave steepness. There is no obvious trend with respect to the two geometries.

From Figs. 8b and 8c, it can be seen that, as observed in the time series data, the NRMS in both surge displacement and pitch angle does not follow such a clear trend with respect to the NRMS in surface elevation. In general, greater NRMS in the incident wave does lead to greater NRMS in both the surge and pitch motion; however, the scatter in the results suggests there are distinct differences in the capabilities of the individual methods, most likely due to inconsistencies in the quality of the implementation. However, it is worth noting that the analysis method used here (normalised RMS) may be better suited to a comparison between surface elevation and heave motion, particularly if the heave is dominated by buoyancy, and alternative quantitative measures of reproduction quality may expose similar trends for the other degrees of freedom. For example, one might expect the surge motion to be dominated by drag forces, so the reproduction might be more strongly linked to the reproduction of the wave velocities, rather than the wave amplitudes.

Figure 9 shows the normalised RMS in the heave displacement versus the CPU effort required to generate the solutions. Here, the CPU effort has been defined as the execution time of the numerical solver, multiplied by the number of cores used in the processing, divided by both the simulated time and the processor speed in GHz. It should be noted that participants were not asked to minimise the CPU effort as part of this study, and any additional "calibration" effort has not been included here (including the effort required to calculate the hydrodynamic coefficients in the linearised methods). Furthermore, the details of the specific hardware used have not been considered here, and this should be remembered when interpreting the results. As is to be expected, the NS solvers require many orders of magnitude more CPU

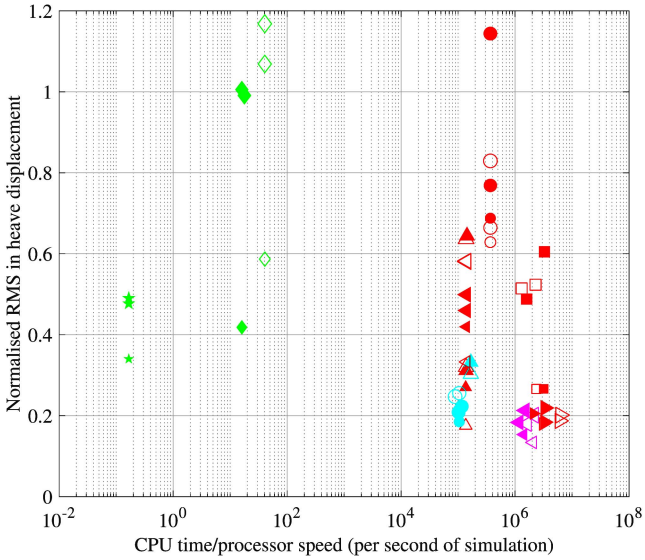

Fig. 9 Normalise RMS error (w.r.t. the experimental data) in the heave displacement vs. CPU effort. Filled markers represent Geometry 1; open markers represent Geometry 2. Marker size scaled by wave steepness, kA. For key, please refer to Fig. 8c.

resources compared to the linearised methods, and in many cases, there is no significant improvement in the prediction to warrant the additional computing cost (for the cases investigated here). The NS solvers with the lowest NRMS (including the PIC method) do also have the highest CPU effort. The NS solvers with the lowest CPU effort also have the widest range in NRMS values and either have a very low number of mesh cells (NS Solver (FDM)) or utilise a fixed time-step (OpenFOAM (source-term) and NS Solver (FVM)(in-house)). In contrast to Ransley et al. (2019), the hybrid methods do now demonstrate a potential improvement in the required CPU effort when compared to the better NS solvers.

CONCLUSIONS

The CCP-WSI Blind Test Series 3 consists of a series of test cases involving focused wave interactions with two separate floating structures: a hemispherical-bottomed buoy and a cylinder with moonpool; the incident waves are varied in steepness but remained unbroken; the structures are taut-moored with a single linear spring mooring. The aims of the study are to assess the numerical codes currently in use, provide a better understanding of the required model fidelity in WSI simulations, help to inform the development of future numerical modelling standards, and to encourage the practical application of these tools by industry.

Ten different codes are used in the test, including a range of underlying complexities from LPT to NS solvers, mesh-based and particle methods, hybrid/coupled methods, and both in-house and open-source codes. No fully nonlinear potential flow solutions are available, so a gap exists in the model fidelities considered. In general, as may be expected, the prediction of heave displacement, which is commonly considered to be a linear response, is reasonably good across all models. There is, however, some evidence that NS solvers provide more accurate results for surge and pitch motion, suggesting these represent a level of complexity that is appropriate to differentiate the predictive capability of different fidelity codes, i.e., include nonlinear effects. In contrast to Ransley et al. (2019), there does appear to be a gradual reduction in the predictive capability as a function of wave steepness, but it is still believed that test cases need to cover a step-change in

physical phenomena, e.g., unbroken/broken wave cases, to make a clear distinction between the predictive capability of numerical models. In the cases considered here, inclusion of a moonpool does not appear to represent sufficient additional complexity to make a distinction; however, it should be noted that the hydrodynamic behaviour of the internal water volume is likely to depend strongly on the incident wave frequency, and other frequencies closer to the internal resonance may give different results. For the NS solvers, it is shown that the quality of the predicted motion of the structures depends strongly on the quality of the surface elevation reproduction in the empty tank case; in the context of heave, it appears that all methods are equally good at predicting the motion given the same quality of incident wave reproduction. The relationships in the other degrees of freedom are less obvious and are likely to be more sensitive to discrepancies in the hydrodynamic predictions, compared to heave motion. As discussed in Ransley et al. (2019), further work is required to establish more appropriate analysis strategies for these degrees of freedom, but in order to draw clear conclusions, it may be important to compare numerical solutions at the level of hydrodynamics forces, or the pressure, instead of "integrated quantities" such as wave-induced motions.

Finally, a key observation is that there is considerable scatter in the predictions made by "similar" NS codes, largely attributed to inconsistencies in the model implementation, and this highlights a large risk to end-users and the need for standardised practice in numerical modelling (including the derivation of model uncertainties) for both industrial usage and future comparative studies.

ACKNOWLEDGEMENTS

The CCP-WSI Working Group acknowledges the CCP-WSI Blind Test Series 3 participants for their contributions as well as the ISOPE and IHC for supporting the Blind Test as part of the ISOPE conference series. This work is funded by the Engineering and Physical Sciences Research Council (EPSRC) through projects EP/M022382/1, EP/S000747/1, and EP/P026109/1. The full physical data set from the CCP-WSI Blind Test Series 3 is available as a long-standing test case for future benchmarking and can be downloaded from http://www.ccp-wsi.ac.uk/data_repository/test_cases/test_case_005.

REFERENCES

Bingham, H (2019). *DTUMotionSimulator package*, Technical University of Denmark, Kongens Lyngby, Denmark.

Brown, SA, Musiedlak, P-H, Ransley, EJ, and Greaves, DM (2019). "Numerical Investigation of Focused Wave Impacts on Floating Wave Energy Converters Using OpenFOAM," *Proc 29th Int Ocean Polar Eng Conf*, Honolulu, HI, USA, ISOPE, 3, 3044–3050.

Chen, H, Qian, L, Ma, Z, Bai, W, Li, Y, Causon, D, and Mingham, C (2019a). "Application of an Overset Mesh Based Numerical Wave Tank for Modelling Realistic Free-Surface Hydrodynamic Problems," *Ocean Eng*, 176, 97–117. https://doi.org/10.1016/j.oceaneng.2019.02.001.

Chen, H, Qian, L, Ma, Z, Bai, W, and Lin, Z (2019b). "CCP-WSI Blind Test Series 3: OpenFOAM Simulation of Focused Wave Interaction with a Simplified Wave Energy Converter," *Proc 29th Int Ocean Polar Eng Conf*, Honolulu, HI, USA, ISOPE, 3, 3096–3101.

Chen, Q, Kelly, DM, and Zang, J (2019). "On the Relaxation Approach for Wave Absorption in Numerical Wave Tanks," *Ocean Eng*, 187, 106210. https://doi.org/10.1016/j.oceaneng.2019.106210.

Chen, Q, Zang, J, Ning, D, Blenkinsopp, C, and Gao, J (2019). "A 3D Parallel Particle-in-cell Solver for Extreme Wave Interaction with Floating Bodies," *Ocean Eng*, 179, 1–12. https://doi.org/10.1016/j.oceaneng.2019.02.047.

Cheng, L, Zheng, J, Gu, H, and Gong, X (2019). "Focused Wave Interaction with Floating Structures by In-house Codes," *Proc 29th Int Ocean Polar Eng Conf*, Honolulu, HI, USA, ISOPE, 3, 3102–3107.

Giorgi, G (2019). "CCP-WSI Blind Test Series 3: A Nonlinear Froude-Krylov Modelling Approach," *Proc 29th Int Ocean Polar Eng Conf*, Honolulu, HI, USA, ISOPE, 3, 3073–3080.

Giorgi, G, and Ringwood, JV (2018a). "Analytical Representation of Nonlinear Froude-Krylov Forces for 3-Dof Point Absorbing Wave Energy Devices," *Ocean Eng*, 164, 749–759. https://doi.org/10.1016/j.oceaneng.2018.07.020.

Giorgi, G, and Ringwood, JV (2018b). "Relevance of Pressure Field Accuracy for Nonlinear Froude–Krylov Force Calculations for Wave Energy Devices," *J Ocean Eng Mar Energy*, 4(1), 57–71. https://doi.org/10.1007/s40722-017-0107-5.

Hann, M, Greaves, D, and Raby, A (2015). "Snatch Loading of a Single Taut Moored Floating Wave Energy Converter due to Focused Wave Groups," *Ocean Eng*, 96, 258–271. https://doi.org/10.1016/j.oceaneng.2014.11.011.

Higuera, P, Lara, JL, and Losada, IJ (2013). "Realistic Wave Generation and Active Wave Absorption for Navier-Stokes Models: Application to OpenFOAM®," *Coastal Eng*, 71, 102–118. https://doi.org/10.1016/j.coastaleng.2012.07.002.

Hinrichsen, PF (2014). "Bifilar Suspension Measurement of Boat Inertia Parameters," *J Sailboat Technol*, Article 2014-01.

Jacobsen, N, Fuhrman, D, and Fredsøe, J (2012). "A Wave Generation Toolbox for the Open-source CFD Library: OpenFOAM®," *Int J Numer Methods Fluids*, 70(9), 1073–1088. https://doi.org/10.1002/fld.2726.

Li, Q, Yan, S, Wang, J, and Ma, Q (2018). "Numerical Simulation of Focusing Wave Interaction with FPSO-like Structure Using FNPT-NS Solver," *Proc 28th Int Ocean Polar Eng Conf*, Sapporo, Japan, ISOPE, 1, 1458–1464.

Lin, P, Cheng, L, and Liu, D (2016). "A Two-phase Flow Model for Wave-structure Interaction Using a Virtual Boundary Force Method," *Comput Fluids*, 129, 101–110. https://doi.org.10.1016/j.compfluid.2016.02.007.

Liu, D, and Lin, P (2009). "Three-dimensional Liquid Sloshing in a Tank with Baffles," *Ocean Eng*, 36(2), 202–212. https://doi.org/10.1016/j.oceaneng.2008.10.004.

Liu, Z, Zhuang, Y, Wan, D, and Chen, G (2019). "Numerical Study on Focused Wave Interactions with a Moored Floating Structure," *Proc 29th Int Ocean Polar Eng Conf*, Honolulu, HI, USA, ISOPE, 3, 3081–3088.

Ma, QW, and Yan, S (2006). "Quasi ALE Finite Element Method for Nonlinear Water Waves," *J Comput Phys*, 212(1), 52–72. https://doi.org/10.1016/j.jcp.2005.06.014.

Ma, QW, and Yan, S (2009). "QALE-FEM for Numerical Modelling of Non-Linear Interaction Between 3D Moored Floating Bodies and Steep Waves," *Int J Numer Methods Fluids*, 78(6), 713–756. https://doi.org/10.1002/nme.2505.

Park, JC, Kim, MH, and Miyata, H (1999). "Fully Non-linear Free-surface Simulations by a 3D Viscous Numerical Wave Tank," *Int J Numer Methods Fluids*, 29(6), 685–703. https://doi.org/10.1002/(SICI)1097-0363(19990330)29:6<685::AID-FLD807>3.0.CO;2-D.

Ransley, E, Greaves, D, Raby, A, Simmonds, D, and Hann, M (2017). "Survivability of Wave Energy Converters Using CFD," *Renewable Energy*, 109, 235–247. https://doi.org/10.1016/j.renene.2017.03.003.

Ransley, E, Jones, C, et al. (2016). *Wave Structure Interaction Computation and Experiment Roadmap Part 1: A Report on the 1st CCP-WSI Focus Group Workshop*, PEARL Research Repository. https://doi.org/10.24382/zw9p-t026.

Ransley, E., et al. (2019). "A Blind Comparative Study of Focused Wave Interactions with a Fixed FPSO-like Structure (CCP-WSI Blind Test Series 1)," *Int J Offshore Polar Eng*, ISOPE, 29(2), 113–127. https://doi.org/10.17736/ijope.2019.jc748.

Rusche, H (2002). *Computational Fluid Dynamics of Dispersed Two-Phase Flows at High Phase Fractions*, PhD Thesis, Imperial College of Science, Technology and Medicine, London, UK.

Schmitt, P, and Elsaesser, B (2015). "A Review of Wave Makers for 3D Numerical Simulations," *MARINE 2015 – Computational Methods in Marine Engineering VI*, Rome, Italy, 437–446.

Schmitt, P, Windt, C, Davidson, J, and Ringwood, J (2019). "The Efficient Application of an Impulse Source Wave Maker to CFD Simulations," *J Mar Sci Eng*, 7(3), 71. https://doi.org/10.3390/jmse7030071.

Tromans, PS, Anaturk, AR, and Hagemeijer, P (1991). "A New Model for the Kinematics of Large Ocean Waves - Application as a Design Wave," *Proc 1st Int Offshore Polar Eng Conf*, Edinburgh, UK, ISOPE, 3, 64–71.

WAMIT (2019). *WAMIT User Manual Version 7.3*, Wamit Inc, Chestnut Hill, MA, USA.

Wang, J, Zhao, W, and Wan, D (2019). "Development of naoe-FOAM-SJTU Solver Based on OpenFOAM for Marine Hydrodynamics," *J Hydrodyn*, 31(1), 1–10. https://doi.org/10.1007/s42241-019-0020-6.

Wendt, F, et al. (2019). "Ocean Energy Systems Wave Energy Modelling Task: Modelling, Verification and Validation of Wave Energy Converters," *J Mar Sci Eng*, 7(11), 379. https://doi.org/10.3390/jmse7110379.

Windt, C, Davidson, J, Schmitt, P, and Ringwood, J (2019). "Contribution to the CCP-WSI Blind Test Series 3: Analysis of Scaling Effects of Moored Point-Absorber Wave Energy Converters in a CFD-based Numerical Wave Tank," *Proc 29th Int Ocean Polar Eng Conf*, Honolulu, HI, USA, ISOPE, 3, 3051–3058.

Yan, S, and Ma, QW (2007). "Numerical Simulation of Fully Non-Linear Interaction Between Steep Waves and 2D Floating Bodies Using the QALE-FEM Method," *J Comput Phys*, 221(2), 666–692. https://doi.org/10.1016/j.jcp.2006.06.046.

Yan, S, Wang, J, Wang, J, Ma, Q, and Xie, Z (2020). "CCP-WSI Blind Test using qaleFOAM with an Improved Passive Wave Absorber," *Int J Offshore Polar Eng*, ISOPE, 30(1), 43–52. https://doi.org/10.17736/ijope.2020.jc781.

Zhang, N, Yan, S, Zheng, X, and Ma, Q (2019). "A 3-D Hybrid Model Coupling SPH and QALE-FEM for Simulating Nonlinear Water Wave Interaction with Floating Structure," *Proc 29th Int Ocean Polar Eng Conf*, Honolulu, HI, USA, ISOPE, 3, 3059–3065.

Zheng, X, Ma, Q, and Duan, W (2014). "Incompressible SPH Method Based on Rankine Source Solution for Violent Water Wave Simulation," *J Comput Phys*, 276, 291–314. https://doi.org/10.1016/j.jcp.2014.07.036.